Anisotropic magnetization plateaus in $S_{eff} = 1/2$ skew-chain single-crystal $Co_2V_2O_7$

L. Yin,[1] Z. W. Ouyang,[1,*] J. F. Wang,[1,†] X. Y. Yue,[1] R. Chen,[1] Z. Z. He,[2] Z. X. Wang,[1] Z. C. Xia,[1] and Y. Liu[3]

[1]*Wuhan National High Magnetic Field Center & School of Physics, Huazhong University of Science and Technology,*
Wuhan 430074, People's Republic of China
[2]*State Key Laboratory of Structural Chemistry, Fujian Institute of Research on the Structure of Matter,*
Chinese Academy of Sciences, Fuzhou 350002, People's Republic of China
[3]*School of Physics and Technology, Wuhan University, Wuhan 430072, People's Republic of China*

We report anisotropic magnetization plateaus in the skew-chain antiferromagnet $Co_2V_2O_7$ with $S_{eff} = 1/2$ and a large g factor. When the field is applied along the easy b axis, a 1/2-like magnetization plateau is observed within 5.4∼11.6 T, followed by a 3/4 plateau at 15.7 T. For the hard a and c axes, however, there is only a sign of 1/2-like magnetization plateau. These observations are quite different from the isostructural $Ni_2V_2O_7$ [Z. W. Ouyang *et al.*, Phys. Rev. B **97**, 144406 (2018)]. Theoretically, the first-principles calculations reveal the large interchain coupling, which leads to classical antiferromagnetic ordering and spin-flop-like transition. With this large interchain coupling, the exact diagonalization analysis yields 1/2 and 3/4 plateaus, showing the quantum origin of magnetization plateaus. Thus, $Co_2V_2O_7$ is an interchain-coupled system showing both classical and quantum behaviors.

I. INTRODUCTION

Quantum effects in classical antiferromagnets are very interesting. One example of great concern is magnetization plateau, in which the magnetization corresponds to a fraction of saturation magnetization—M_s/n, where n is the period of the spin state [1]. Not surprisingly, magnetization plateaus of pure quantum origin can be observed in low-dimensional (D) quantum spin systems like diamond chain [2], bond-alternating chain [3], ladders [4], and spin dimers [5], in which the spin number is small ($S \leqslant 1$) and the long-range antiferromagnetic (AFM) ordering is absent due to quantum fluctuations. For the triangular, kagome, and pyrochlore lattices, the 1/3 or 1/2 magnetization plateau can occur in both quantum [6] and classical systems [7–13] with spin number varying from $S = 1/2$ to 5/2, because spin configurations can be stabilized by thermal and/or quantum fluctuations due to geometrical frustration or spin-lattice coupling. Interestingly, the coupled $S = 1/2$ spin clusters [14–16] were found to have a coexistence of quantum-mechanical magnetization plateau and AFM long-range ordering. The trimerlike $SrMn_3P_4O_{14}$ ($S = 5/2$) [17] can be considered as an extreme example which exhibits 1/3 plateau in a classical large-spin system.

In most of the chainlike low-D systems exhibiting magnetization plateau, the interchain coupling is negligible or at least not dominant. Otherwise, the quantum magnetization plateau is not expected to occur. However, we have recently observed a 1/2 magnetization plateau and a nematiclike transition in the $S = 1$ skew-chain system $Ni_2V_2O_7$ [18]. This observation is indeed unusual for a system exhibiting classical AFM

ordering and spin-flop transition due to large interchain coupling [19,20].

There is an isostructural skew-chain antiferromagnet $Co_2V_2O_7$ [21–23]. As shown in Fig. 1(a), $Co_2V_2O_7$ has a monoclinic crystal structure (space group $P21/c$) [21,24] composed of skew chains of edge-sharing octahedra, $Co(I)O_6$ and $Co(II)O_6$, running along the c axis of the crystal. The quasi-one-dimensional structure is formed by embedding the corner-shared nonmagnetic tetrahedrons VO_4 [not shown in Fig. 1(a) for clarity] in between the skew chains. It was reported that $Co_2V_2O_7$ undergoes an AFM ordering at $T_N = 6$ K [25] and a field-induced spin-flop-like transition along the b axis. Obviously, Co^{2+} ions display three-dimensional (3D) magnetism due to the interchain coupling, similar to the isostructural $Ni_2V_2O_7$ [19,20]. Very recently, a sign of 1/2 magnetization plateau has been observed between 7 and 12 T in $Co_2V_2O_7$ [26]. Note that this plateau is not as flat as that in $Ni_2V_2O_7$ [18] even after subtracting the Van Vleck paramagnetic susceptibility. This is probably because of the use of polycrystalline samples. Also, there is a very tiny anomaly between 15 and 20 T in the derivative dM/dH curve [26]. All these suggest that consecutive magnetic transitions may occur along the easy axis of $Co_2V_2O_7$.

In this paper, we present anisotropic magnetization process in a single crystal of $Co_2V_2O_7$. Quite different from the case of $Ni_2V_2O_7$ [18], two fascinating magnetization plateaus–a 1/2-like plateau and a 3/4 plateau, are observed, depending on crystallographic directions. Our high-field magnetization and electron spin resonance (ESR) data demonstrate the validation of $S_{eff} = 1/2$ description of the magnetic moment with a large g factor at low temperature. The first-principles calculations and exact diagonalization are employed to explain the large interchain coupling and the unusual magnetization process.
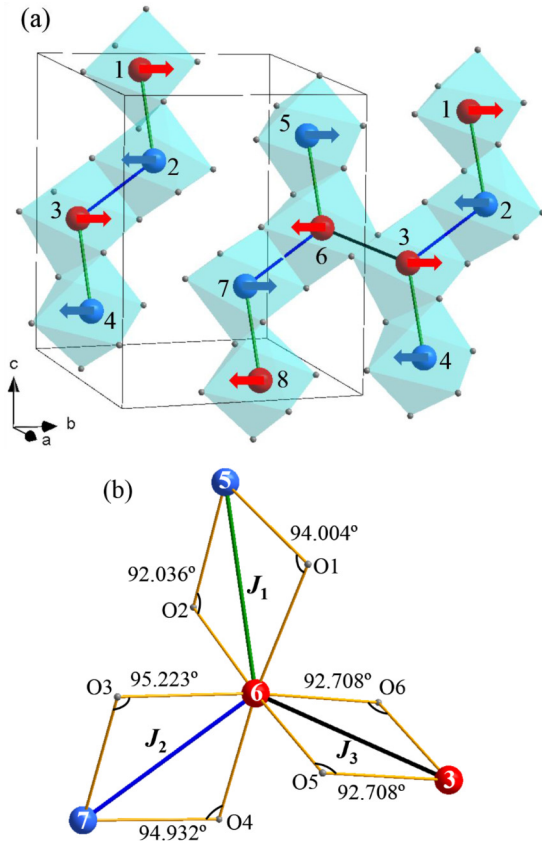
*zwouyang@mail.hust.edu.cn
†jfwang@hust.edu.cn

134434-1

FIG. 1. (a) Skew chain with alternating Co(I)O$_6$ (red) and Co(II)O$_6$ (blue) octahedra along the c axis. There are four Co(I) atoms numbered by 1, 3, 6, and 8 and four Co(II) atoms numbered by 2, 4, 5, and 7 in a unit cell (4 formula unit). The arrows denote the spin orientations of Co ions for the ground-state AFM-1 derived from the first-principles calculations. (b) Three types of superexchange interactions: J_1—3.053(3) Å (green bond, Co5-O1/O2-Co6), J_2—3.033(5) Å (blue bond, Co6-O3/O4-Co7), and J_3—2.972(7) Å (black bond, Co3-O5/O6-Co6) as well as the Co–O–Co bond angles.

II. EXPERIMENTAL DETAILS

The single crystal of Co$_2$V$_2$O$_7$ was prepared by the published procedures [25]. The polycrystalline powder was synthesized by a standard solid-state reaction method. Single-crystal x-ray-diffraction (XRD) data were collected at room temperature using the program SHELXL-2016 on an XtaLAB Mini II diffractometer equipped with a Rigaku Mo x-ray source. Powder XRD data were collected using a PANalytical X'Pert powder x-ray diffractometer with Cu Kα radiation. The program FULLPROF was used for the Rietveld refinement [27]. The chemical compositions were checked by an electron probe microanalyzer (EPMA-8050G). Magnetization measurements were performed with a superconducting quantum interference device (SQUID) magnetometer. Specific heat was measured under 0–7 T using a commercial physical properties measurement system (PPSM). High-field magnetization measurements were performed at 0.7–7 K using a homemade pulsed field up to 38 T. The pulsed-field ESR spectra were collected in the field-increasing process. The first-principles calculations were carried out using the self-consistent full potential linearized augmented plane-wave package WIEN2K [28],
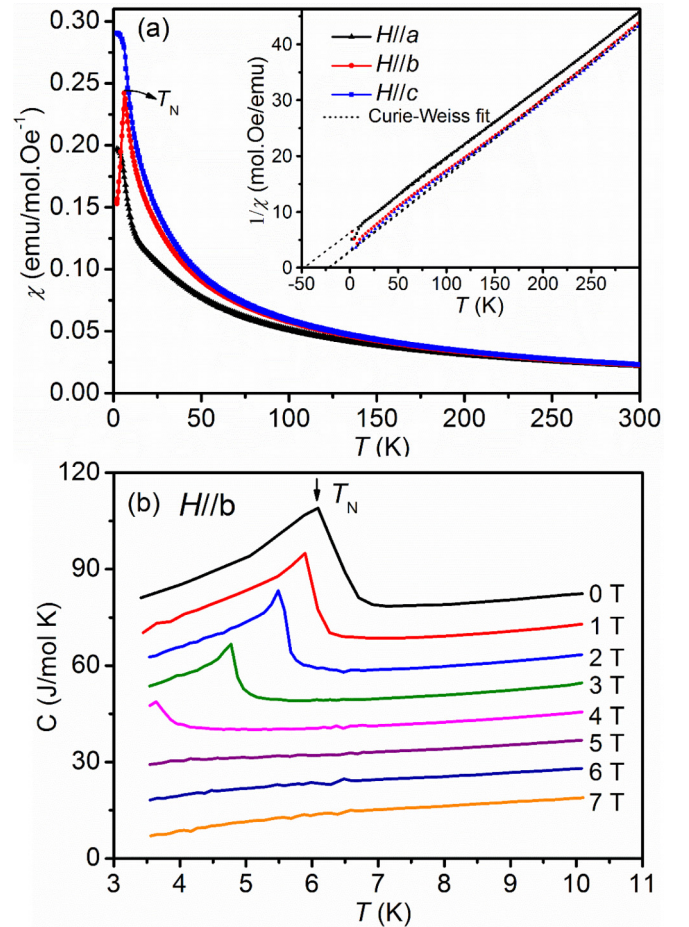

FIG. 2. (a) Magnetic susceptibility $\chi(T)$ curves measured at 0.1 T. The inset is the corresponding $\chi^{-1}(T)$ curves. The dashed lines represent Curie-Weiss fit. (b) Specific heat curves for $H//b$ measured at different fields. The curves are shifted up by various magnitudes in relation to the 7-T curve.

using the general gradient approximation with the Perdew-Burke-Ernzerhof [29] parametrization for the exchange correlation. The considered spin configurations are collinear. To include the correlated effect of 3d electrons, the effective on-site Coulomb interaction parameter was chosen as $U_{\mathrm{eff}} = U - J = 5.0$ eV for Co^{2+} [30,31], where U and J are on-site Coulomb and exchange interactions, respectively. A mesh of 150 k points was used in the first Brillouin zone. The self-consistency was achieved by demanding the convergence of total energy to be smaller than 1 meV.

III. RESULTS AND DISCUSSION

A. Anisotropic magnetization plateaus

Figure 2(a) shows the temperature-dependent magnetic susceptibility $\chi(T)$ of single-crystal Co$_2$V$_2$O$_7$ measured at 0.1 T. The susceptibility is isotropic at high temperature but is highly anisotropic at low temperature. Similar to the previous report [25], the $\chi(T)$ curve exhibits a sharp cusp at the AFM ordering temperature of $T_N \sim 6.0$ K when the magnetic field is applied along the easy b axis ($H//b$). For the hard a and c axes, however, a small increase in susceptibility is seen below

T_N. The $\chi^{-1}(T)$ curves shown in the inset of Fig. 2(a) follows the Curie-Weiss law above ∼150 K with a paramagnetic Curie temperature $\theta_p = -46$, -19, and -20 K for a, b, and c axes, respectively. The corresponding effective moment is 5.6, 5.8. and 5.4 μ_B/Co^{2+}, close to the previous reports [22,25]. Note that below 150 K, the $\chi^{-1}(T)$ curves deviate from the Curie-Weiss law, which implies the presence of short-range spin correlations well above T_N.

The magnetic phase transitions can be further confirmed by specific heat measurements. Figure 2(b) shows the $C(T)$ curves for $H//b$ measured at different fields. As expected, a sharp λ-like peak is seen at $T_N \sim 6.0$ K in the zero-field curve. As the magnetic field increases, the λ-like peak shifts to the lower temperature, which is a typical feature for classical antiferromagnet. The vanishing of the λ-like peak above 5 T suggests that the AFM state is suppressed and a new spin state appears in the high field.

Figure 3(a) shows the high-field magnetization $M(H)$ curves measured at 1.7 K for single-crystal $Co_2V_2O_7$. The absolute values of magnetization are calibrated with SQUID data. The magnetization process is highly anisotropic. All the curves present complicated field-induced magnetic transitions (see, e.g., the dM/dH curve for the b axis). Note that the high-field magnetization increases linearly for all three crystallographic directions due to the Van Vleck paramagnetism of Co^{2+} originating from the contribution of excited states in the octahedral environment [32,33]. From the slope of the $M(H)$ curve, the Van Vleck paramagnetic susceptibility is evaluated as $\chi_{VV} = 0.022$, 0.027, and $0.010(\mu_B/T)/Co^{2+}$ for a, b, and c axes, respectively. These values are comparable to those in other Co-based systems exhibiting a magnetization plateau and a similar Van Vleck effect [10,34]. Interestingly, an extrapolation of the linear part to zero field points to the same magnetization, suggesting that the saturation magnetization is the same for all three axes.

To better examine the anisotropic magnetization process, we plot in Fig. 3(b) the $M(H)$ and the normalized M/M_s curves corrected for the Van Vleck term. The saturation magnetization is determined as $M_s = 2.05$ μ_B/Co^{2+}. For the hard axes, the $M(H)$ curve is composed of two anomalies at ∼6.8 and 18.6 T for $H//a$ (black line) and ∼7.8 and 23.3 T for $H//c$ (blue line), respectively. Between the two anomalies, the magnetization increases smoothly with an upward curvature, signaling the existence of a 1/2-like magnetization plateau. The case is more complicated when the field is applied along the easy b axis (red line). In low field, a spin-flop-like transition is seen at ∼3.0 T from the maximum of dM/dH [see Fig. 3(a)], similar to the previous report [25]. Interestingly, between $H_{c1} = 5.4$ T and $H_{c2} = 11.6$ T, the magnetization remains nearly unaltered and a 1/2-like magnetization plateau is well established. The plateau magnetization is about 1.07 μ_B/Co^{2+}, which is close to $1/2M_s$. With further increasing the magnetic field from H_{c2}, there is a fast increase in magnetization followed by an anomaly at $H_{c3} = 15.7$ T. The magnetization at H_{c3} is estimated as 1.54 μ_B/Co^{2+}, equal to $3/4M_s$. Above $H_{c4} = 20.2$ T, the magnetization reaches saturation. Figure 4 shows the raw $M(H)$ curves for $H//b$ measured at 0.7-7 K. As temperature rises, H_{c1} and H_{c4} move towards lower field, whereas H_{c2} shifts to higher field. There is no significant shift for H_{c3}. Above $T_N = 6$ K, all anomalies
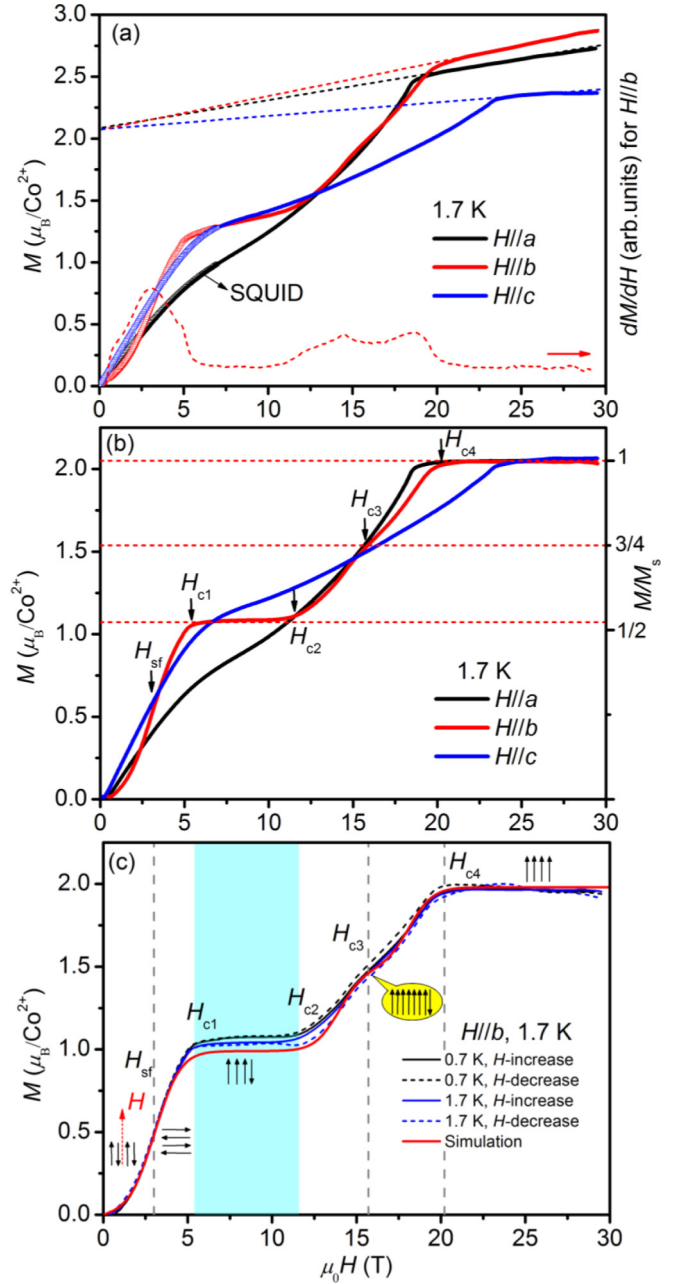

FIG. 3. (a) High-field $M(H)$ curves (left) measured at 1.7 K and dM/dH for the b axis (right). The absolute values of magnetization are calibrated with SQUID data (symbols). The dashed straight lines represent the linear extrapolation of the curves to zero field. (b) $M(H)$ (left) and normalized M/M_s curves (right) corrected for the Van Vleck term. The dashed straight lines mark the magnetization between H_{c1} and H_{c2}, at H_{c3}, and above H_{c4}. (c) A comparison of the experimental $M(H)$ curve at 0.7 and 1.7 K for the b axis with the calculated $M(H)$ curve with $g = 3.95$, $J_1 = -17.1$ K, $J_2 = -30.1$ K, and $J_3 = -13.9$ K. The arrows show the field direction and possible spin structures at various states.

disappear and the curve presents a typical paramagnetic behavior.

The magnetic anisotropy can be described by the molecular-field model, in which the spin-flop transition field
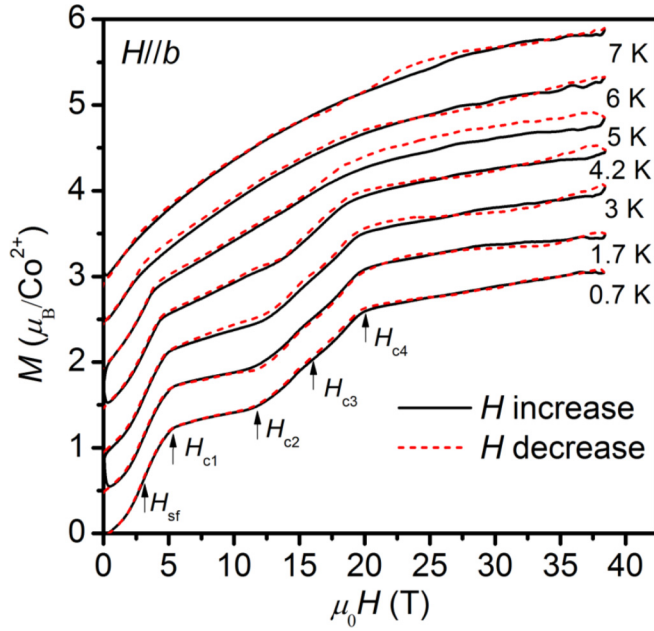
FIG. 4. Field-increasing and decreasing $M(H)$ curves for $H//b$ measured from 0.7 to 7 K.

H_{sf} and the saturation field H_{c4} are expressed as [35]

$$H_{sf} = \sqrt{(2H_E - H_A)H_A} \qquad (1)$$

$$H_{c4} = 2H_E - H_A \qquad (2)$$

With $H_{sf} = 3.0$ T and $H_{c4} = 20.2$ T, the exchange field is derived to be $H_E = 10.3$ T (13.9 K) and the anisotropic field $H_A = 0.45$ T (0.6 K), which indicates a magnetic anisotropy.

The g factor is important for theoretical analysis of magnetization plateaus (see below). Note that effective magnetic moments of 5.29 μ_B/Co^{2+} for polycrystals [25] and 5.4–5.8 μ_B/Co^{2+} for our single crystal have been derived from the high-temperature magnetic susceptibility. These values are much larger than theoretical value of 3.87 μ_B/Co^{2+} with $S = 3/2$ and $g = 2.0$, showing a large contribution of orbital moment. This is the case at high temperature. Based on the crystal-field theory, the Co^{2+} ion located in an octahedral environment is in high-spin ($S = 3/2$) state at room temperature. However, when the temperature is much lower than $|\lambda|/k_B \approx 250$ K (λ is the spin-orbit coupling constant) [32,33], the system can be described by an effective spin of $S_{eff} = 1/2$ with total g factors of about 13 for three different field directions [10]. With $S_{eff} = 1/2$ and experimental value of $M_s = g\mu_B S_{eff}$, the g factor is determined as $g = 4.10$, which is much smaller than $g = 5.2$ estimated by high-field magnetization data of powder sample [26]. This is obviously due to the difference in saturation magnetization. See Appendixes A and B for details.

The ESR is known to be a precise technique to determine the g value. Our high-field ESR measurements show that at high temperature well above T_N, a single peak is observed and it can be ascribed to the paramagnetic resonance. The peak is very broad because of the presence of short-range spin
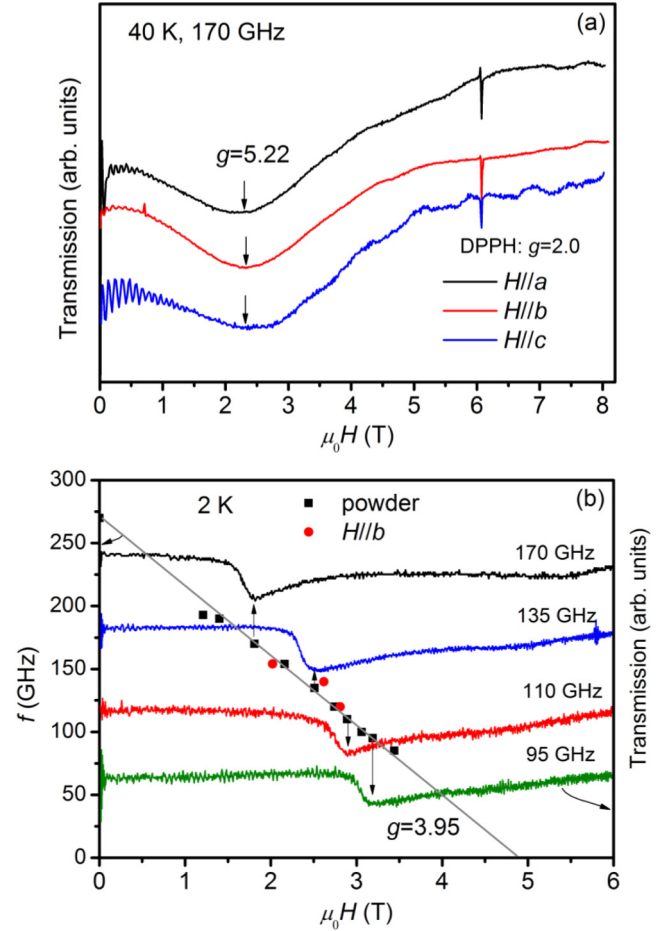

FIG. 5. (a) ESR spectra of single crystal measured at 170 GHz and 40 K. The sharp DPPH line ($g = 2.0$) is used for a field marker. (b) Frequency-field (f-H) relation at 2 K as well as several representative ESR spectra of powder sample.

correlations, in line with the result of $\chi^{-1}(T)$ in Fig. 2(a). Figure 5(a) shows the ESR spectra measured at 170 GHz at 40 K along the three axes, where the sharp diphenylpicrylhydrazyl (DPPH) line ($g = 2.0$) is for a field marker. There is no significant change of the resonance field for the three directions and thus the g value is derived to be $g = 5.22$.

At low temperature, a shift of g factor is possible due to the AFM ordering. Unfortunately, the ESR spectrum at 2 K ($<T_N = 6$ K) exhibits a multiple-peak structure (not shown here for clarity), which prevents us from determining the g value. However, at low field and low frequency, we observed a special AFM resonance mode whose resonance field decreases with increasing frequency. The intensity of this mode is strong for the powder sample but weak for the tiny single crystal. We plot in Fig. 5(b) the frequency-field (f-H) relation at 2 K as well as several representative ESR spectra of powder sample. Clearly, the f-H relation is linear and can be described by $hf/g\mu_B = \Delta - H$ with $g = 3.95$ and zero-field gap of $\Delta = 270$ GHz (i.e., 4.88 T). The value of Δ reflects the magnitude of H_E and H_A. As seen from Fig. 5(b), extrapolation of the f-H relation to high field shows that this mode becomes soft at 4.88 T, which is significantly

larger than the spin-flop transition field of $H_{sf} = 3.0$ T, i.e., $(2H_E \cdot H_A)^{1/2}$, but close to the critical field for the onset of 1/2 plateau. To clarify the origin of this ESR mode, detailed high-field ESR studies are desired. Our high-field magnetization and ESR data unequivocally show that $Co_2V_2O_7$ indeed has a large g factor. Thus, the $S_{eff} = 1/2$ description of the magnetic moment is valid at low temperature. The obtained $g = 3.95$ at 2 K from ESR spectra should be more reliable compared with those estimated by high-field magnetization calibrated with SQUID data and corrected by subtracting Van Vleck paramagnetism. We also note that a comparable value of $g = 3.84$–3.87 was reported in the Co-based quantum magnet $Ba_3CoSb_2O_9$ which has $S_{eff} = 1/2$ and exhibits a 1/3 magnetization plateau at low temperature [10].

So far, we have illustrated the presence of a well-defined 1/2-like magnetization plateau and a 3/4 plateau, depending on crystallographic axes, in the skew-chain antiferromagnet $Co_2V_2O_7$ which has $S_{eff} = 1/2$ and a large g factor at low temperature. The observation of magnetization plateaus is quite different from the isostructural $Ni_2V_2O_7$ [18], where a well-defined 1/2 plateau was observed along all three directions. In $Ni_2V_2O_7$, there are two easy magnetization directions, a and b axes, and thus two spin-flop-like transitions. The ground-state spins are aligned within the ab plane and a spin nematiclike transition appears [18]. In $Co_2V_2O_7$, however, there is only one easy axis, one spin-flop-like transition, and thus no spin nematiclike phase.

As compared with the powder sample of $Co_2V_2O_7$ exhibiting a sign of 1/2 magnetization plateau within 7–12 T and a very tiny anomaly between 15 and 20 T in the dM/dH curve [26], the plateaus in single crystal are strongly anisotropic. In particular, the 1/2-like magnetization for the easy b axis is extremely flat within a more broad field range of 5.4~11.6 T. The 3/4 plateau appears only along the b axis. Note that the ESR spectra give a precise value of $g = 3.95$ at 2 K for both single-crystal and powder samples [Fig. 5(b)]. This value corresponds to $M_s = 1.98$ μ_B/Co^{2+}. Thus, the saturation magnetization (2.05 μ_B/Co^{2+}) obtained from single crystal is more reliable than the result (2.6 μ_B/Co^{2+}) of powder sample [26], which is sample dependent (see Appendix B). These are the advantages of single crystal relative to the powder average.

B. Theoretical calculations

Since the $S_{eff} = 1/2$ description of the magnetic moment is valid at low temperature, the observed magnetization plateaus in $Co_2V_2O_7$ could be quantum origin. The interpretation of magnetization plateaus relies on information of exchange interactions. In the following, we first carried out first-principles calculations with the reported structural parameters [25] by considering five types of collinear spin configurations. Table I gives the details of each spin configuration in a unit cell (4 formula unit) containing eight atoms, i.e., four Co(I) atoms numbered by 1, 3, 6, and 8 and four Co(II) atoms numbered by 2, 4, 5, and 7 (see also Fig. 1). As can be seen from Table I, the calculated spin moment is identical for Co(I) and Co(II) and the saturated moment is 2.7 μ_B/Co^{2+}, higher than the experimental value of 2.05 μ_B/Co^{2+}. This discrepancy might be associated with the choice of the U_{eff} term and/or the parameter for the exchange correlation. The AFM-1 state

TABLE I. Total energy (E) relative to the AFM-1 state for the five various spin configurations, one ferromagnetic (FM) and four AFM states, in a unit cell (4 f.u.) containing four Co(I) numbered by 1, 3, 6, and 8 and four Co(II) numbered by 2, 4, 5, and 7 [see Fig. 1(a)]. The arrows "↑" and "↓" represent the relative spin orientations of Co ions in order of Co1, Co2, …Co8.

Configurations	E (meV)	M_{Co} (μ_B)
FM (↑↑↑↑↑↑↑↑)	12.2	2.70
AFM-1 (↑↓↑↓↑↓↑↓)	0.0	2.70
AFM-2 (↑↑↑↑↓↓↓↓)	80.9	2.70
AFM-3 (↑↓↑↓↓↑↓↑)	163.2	2.70
AFM-4 (↑↑↑↓↓↓↑↑)	23.7	2.70

is most stable in energy and can be considered as the ground state, similar to the case of $Ni_2V_2O_7$ [20]. In this state, the exchanges are AFM along the alternating aligned Co(I)-Co(II)-Co(I)-Co(II) chain (J_1 and J_2) and between the nearest-neighboring interchain Co(I)-Co(I) coupling (J_3), which is shown in Fig. 1(a). It should be stressed that the exact values of exchange interactions are not easy to obtain by mapping energy of different spin configurations to the isotropic Heisenberg model Hamiltonian $H = -\Sigma J_{i,j} S_i S_j$ (here J_{ij} includes all the exchanges between sites i and j) because of the complicated 3D magnetism of $Co_2V_2O_7$, which was tried in our recent calculations of $Ni_2V_2O_7$ [20].

However, a qualitative analysis about J_1, J_2, and J_3 is possible. Figure 1(b) shows the three superexchange interactions and the corresponding bond angles. The intrachain J_1 and J_2 are associated with the Co6-O-Co5 and Co6-O-Co7 paths with bond lengths of 3.053(3) Å (green bond) and 3.033(5) Å (blue bond), respectively. The interchain J_3 is via the Co6-O-Co3 path with a bong length of 2.972(7) Å (black bond). The short interchain distance indicates that J_3 might be comparable to J_1 and J_2. This is supported by our calculations. Figure 6 shows the partial density of states (DOS) of Co $3d$ and O $2p$ for the ground-state AFM-1. For Co3 and Co5 atoms, the majority-spin band below Fermi level is completely occupied while the minority-spin band is only partly occupied. The case is reverse for Co6 atom, giving rise to a negative moment. In the valence band mainly composed of Co $3d$ and O $2p$ states, the O $2p$ orbital hybridizes strongly with the Co $3d$ orbitals for both Co6-O-Co3 and Co6-O-Co5 superexchange paths. It is therefore inferred that the interchain J_3 should be comparable to the intrachain J_1.

Furthermore, we plot in Fig. 7(a) the isosurface of valence electron density at the plane determined by Co5, Co7, Co4, and Co2 [see Fig. 1(a)]. A finite charge distribution crossing the Co-O-Co path is seen, but the distribution via Co6-O-Co3 path (J_3) is relatively weaker than those via Co6-O-Co5 (or Co3-O-Co4) path (J_1) and Co6-O-Co7 (or Co3-O-Co2) path (J_2). Note that in this figure the O atoms associated with the superexchanges are not coplanar. For further comparison, we plot in Figs. 7(b)–7(d) the isosurface of valence electron density in each Co-O-Co plane. Clearly, there is a pronounced charge distribution along the Co6-O-Co3 path [Fig. 7(d)], a little bit weaker than the distributions along the Co6-O-Co5 path [Fig. 7(b)] and Co6-O-Co7 path [Fig. 7(c)]. It is
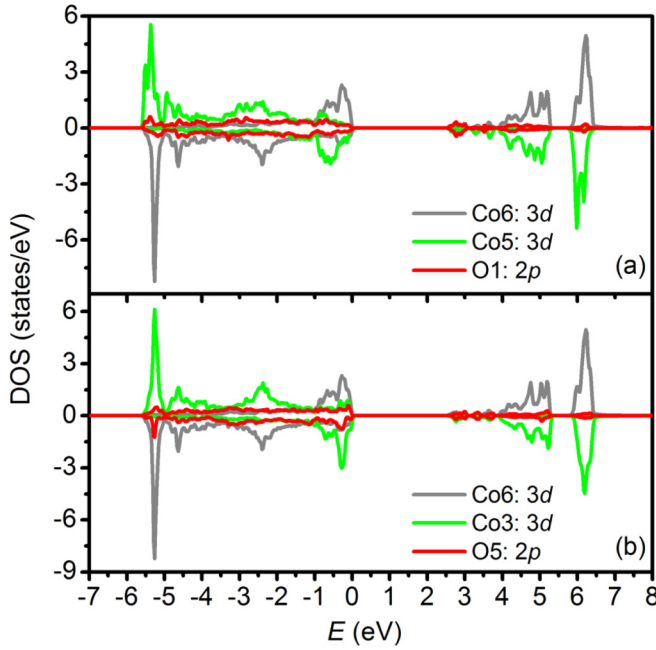
FIG. 6. Partial DOS of Co $3d$ and O $2p$ for the ground-state AFM-1. The Fermi level is at zero energy.

concluded that J_3 is relatively weak but comparable to J_1 and J_2.

With the information that all exchanges are AFM and J_3 is comparable to but smaller than J_1 and J_2, it is possible to simulate the high-field $M(H)$ curves. However, the $M(H)$ curves are highly anisotropic and thus anisotropic exchange interactions should be taken into account, which complicates the simulation. As an approximate treatment, we only attempt to simulate the well-defined 1/2-like magnetization
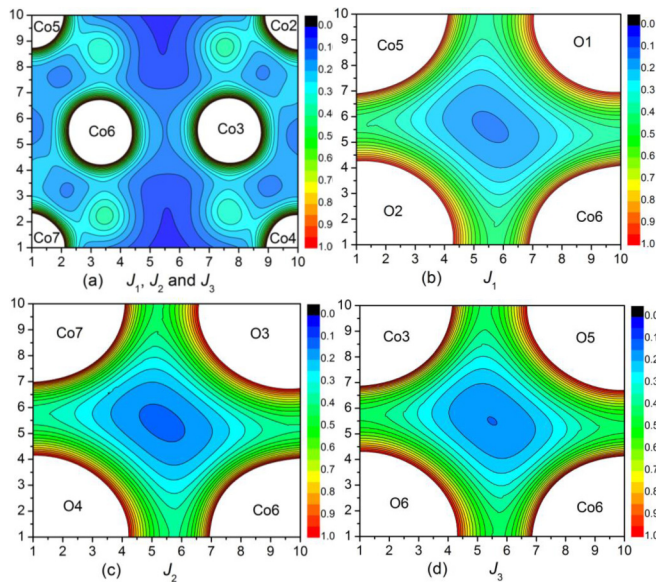

FIG. 7. (a) Isosurface of valence electron density (e Å^{-3}) at the plane determined by Co5, Co7, Co4, and Co2 containing J_1, J_2, and J_3 superexchange paths. (b)–(d) Isosurface of valence electron density for each Co-O-Co plane:J_1—Co6-O-Co5, J_2—Co6-O-Co7, and J_3—Co6-O-Co3.

plateau for the b axis by diagonalizing the Hamiltonian $H = -\Sigma J_{i,j} \mathbf{S}_i \mathbf{S}_j + \Sigma g\mu_B \mathbf{S}_{iz} \mathbf{H}$ with $S_{\text{eff}} = 1/2$ and $g = 3.95$ without including anisotropic exchanges. For simplicity, we consider eight atoms with three interactions J_1, J_2, and J_3. Our simulation shows that the best parameters to describe the magnetization process are $J_1 = -17.1$ K, $J_2 = -30.1$ K, and $J_3 = -13.9$ K. The averaged value is about -19.6 K, which is comparable to the Weiss temperatures θ_p obtained from $\chi^{-1}(T)$. Note that similar treatment can be found in diamond-chain $Cu_3(CO_3)_2(OH)_2$ [2] and triangular-lattice $Ba_3CoSb_2O_9$ [10] which exhibit anisotropic 1/3 magnetization plateaus.

The calculated $M(H)$ curve is given in Fig. 3(c), where the experimental curves for the b axis are also plotted for comparison. The calculated curve produces a well-defined 1/2 magnetization plateau between H_{c1} and H_{c2} and a 3/4 plateau at H_{c2}. Based our simulations, the occurrence of magnetization plateaus is a result of quantum-mechanical discrete energy levels of magnetic eigenstates in spite of the presence of interchain exchange. As seen from the geometrical arrangement of Co ions in Fig. 1, the intrachain and interchain interactions could be frustrated with $f = \theta_p/T_N \sim 3$ [22,25]. It is the quantum fluctuations and frustration that results in the occurrence of plateaus. The possible spin configurations are shown in Fig. 3(c), where the classical spin-flop transition coexists with the quantum magnetization plateaus. The ground-state spins are aligned along the easy b axis with a collinear ↑↓↑↓ spin configuration. Once the spin-flop transition takes place at H_{sf}, the spins become perpendicular to the b axis. As a classical analog, the 1/2 plateau could correspond to a collinear ↑↑↑↓ configuration and the 3/4 plateau a ↑↑↑↑↑↑↑↓ configuration, which can be stabilized by frustration and quantum fluctuations ($S_{\text{eff}} = 1/2$). The exact spin configurations call for further experimental studies using neutron scattering and theoretical calculations containing more Co spins.

Finally, we notice a small discrepancy between the experimental and calculated curves in Fig. 3(c), the exact reason for which is unknown at this moment. The previously reported deviation of the plateau magnetization from the expected $M_s/3$ in kagome lattice $Cu_3V_2O_7(OH)_2 \cdot 2H_2O$ and $BaCu_3V_2O_8(OH)_2$ [36] was later clarified to be due to quality of polycrystalline samples [37]. Recently, 1/2 quantum magnetization plateau was reported in the breathing pyrochlore $Ba_3Yb_2Zn_5O_{11}$ [38]. The magnetization curve is field hysteretic, depending on the field-sweep rate. The plateau magnetization is significantly larger than the calculated curve with conventional Heisenberg spin-exchange Hamiltonian, but close to the adiabatic simulation result. With this in mind, the slight discrepancy of plateau magnetization from $M_s/2$ seen in Fig. 3(c) may, at least in part, be due to the pulse-field magnetization process, which is not completely adiabatic. As shown in Fig. 3(c), the magnitude of discrepancy is different for 0.7 and 1.7 K curves and both present a significant hysteresis between the H-decreasing and H-increasing processes, which is not intrinsic.

IV. CONCLUSIONS

In summary, we have demonstrated the anisotropic magnetization process in $S_{\text{eff}} = 1/2$ skew-chain single-crystal $Co_2V_2O_7$. For the easy b axis, the magnetization curve

consists of a spin-flop-like transition at around 3.0 T, a well-established 1/2-like magnetization plateau within 5.4∼11.6 T, and a 3/4 plateau at 15.7 T. For the hard a and c axes, however, only a sign of 1/2-like plateau is observed, showing a strong magnetic anisotropy. The high-field magnetization and ESR data also demonstrate that $Co_2V_2O_7$ has an effective spin of $S_{eff} = 1/2$ with a large g value. The first-principles calculations reveal that the interchain coupling, which leads to classical AFM ordering and spin-flop-like transition, is comparable to the intrachain couplings. This is further confirmed by exact diagonalization analysis, which yields 1/2 and 3/4 plateaus, confirming the quantum origin of plateaus. Thus, there is coexistence of classical and quantum magnetism.

APPENDIX A: CRYSTAL STRUCTURE AND CHEMICAL COMPOSITION ANALYSIS

Single-crystal XRD analysis shows that $Co_2V_2O_7$ crystallizes in the monoclinic crystal system with space group $P21/c$ [21,24]. The lattice parameters are $a = 6.584(9)$ Å, $b = 8.373(3)$ Å, $c = 9.466(6)$ Å, and $\beta = 100.216(4)°$, in good agreement with the previous report [25]. The powder XRD analysis was performed for the powder sample
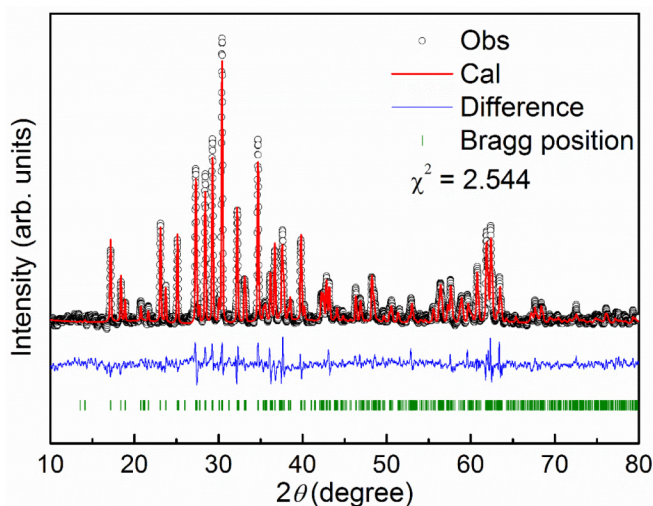

FIG. 8. Observed and calculated powder XRD patterns and the difference between them. The green vertical bars indicate the expected Bragg reflection positions.
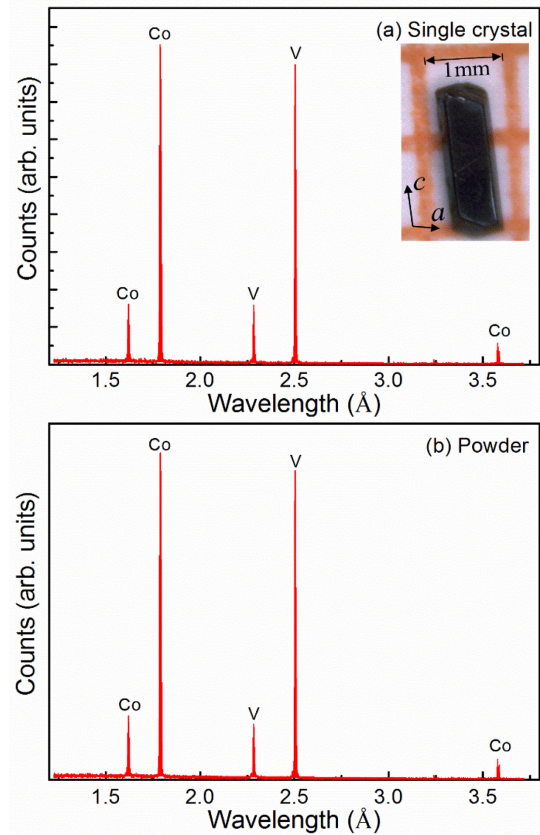

FIG. 9. Energy-dispersive spectrum measured by an EPM for single-crystal and powder samples. The inset shows a photograph of the single crystal.

synthesized by the solid-state reaction method. Figure 8 shows the result of the Rietveld refinement with space group $P21/c$. The calculated patterns match well with the observed patterns. No impurity phase is detected, showing the high quality of powder sample. The refined lattice parameters are $a = 6.644(2)$ Å, $b = 8.444(5)$ Å, $c = 9.554(3)$ Å, and $\beta = 100.329(2)°$, slightly larger than those of single crystal.

Figure 9 shows the energy-dispersive spectrum measured by an electron probe microanalyzer as well as a photograph of the single crystal. Table II lists the details of the chemical composition obtained at two random sites in the samples. The true Co:V:O ratio is quite close to the nominal ratio of 2:2:7 for both single-crystal and powder samples, again showing the high quality of the samples.

TABLE II. The quantitative chemical composition analysis performed by an electron probe microanalyzer for single-crystal and powder samples.

Sample	Site	Co (at. %)	V (at. %)	O (at. %)	Total
Single crystal	Point1	19.192	17.604	63.204	100
	Point2	18.432	18.039	63.529	100
Powder	Point1	18.336	18.094	63.570	100
	Point2	18.711	17.879	63.410	100

APPENDIX B: MAGNETIZATION CURVE OF POWDER SAMPLE

Figure 10 shows the $M(H)$ curve at 2 K for the powder sample using a SQUID magnetometer. As expected, the field-induced spin-flop-like transition is hard to identify in comparison with the single-crystal data along the easy b axis. If the spin-flop transition field is defined as the maximum of the dM/dH, the value of H_{sf} is estimated to be 4.3 T, which is larger than 3.0 T for the b axis [Fig. 3(a)]. No magnetic saturation is reached at 7 T. The magnetization at 7 T is about $1.27\,\mu_B/Co^{2+}$. After subtracting the Van Vleck term whose value is unknown for our sample, the magnetization at 7 T would be significantly smaller than $1.3\,\mu_B/Co^{2+}$ reported recently [26]. Thus, the saturation moment of our sample is smaller than $2.6\,\mu_B/Co^{2+}$ [26], reducing the magnetic difference between powder and single crystal. All these suggest that the magnetization is sample dependent.

For single crystal, the magnetization at 7 T is, respectively, about 0.98, 1.29, and $1.28\,\mu_B/Co^2$ for a, b, and c axes [Fig. 3(a)] without subtraction of the Van Vleck term. The averaged value of $1.18\,\mu_B/Co^2$ is still smaller than $1.27\,\mu_B/Co^{2+}$ of our powder sample. Keep in mind that our single-crystal and powder samples are of high quality. There
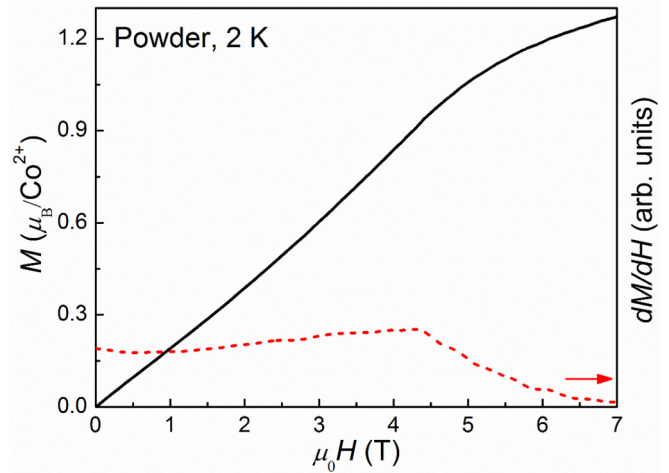

FIG. 10. The $M(H)$ curve measured at 2 K for powder sample.

is a small difference in lattice parameters (see Appendix A). The magnetic difference between single crystal and powder might be associated with the difference in microstructures.

[1] M. Oshikawa, M. Yamanaka, and I. Affleck, Phys. Rev. Lett. **78**, 1984 (1997).

[2] H. Kikuchi, Y. Fujii, M. Chiba, S. Mitsudo, T. Idehara, T. Tonegawa, K. Okamoto, T. Sakai, T. Kuwai, and H. Ohta, Phys. Rev. Lett. **94**, 227201 (2005).

[3] Y. Narumi, K. Kindo, M. Hagiwara, H. Nakano, A. Kawaguchi, K. Okunishi, and M. Kohno, Phys. Rev. B **69**, 174405 (2004).

[4] T. Sugimoto, M. Mori, T. Tohyama, and S. Maekawa, Phys. Rev. B **92**, 125114 (2015).

[5] Y. H. Matsuda, N. Abe, S. Takeyama, H. Kageyama, P. Corboz, A. Honecker, S. R. Manmana, G. R. Foltin, K. P. Schmidt, and F. Mila, Phys. Rev. Lett. **111**, 137204 (2013).

[6] T. Ono, H. Tanaka, H. Aruga Katori, F. Ishikawa, H. Mitamura, and T. Goto, Phys. Rev. B **67**, 104431 (2003).

[7] N. Terada, Y. Narumi, K. Katsumata, T. Yamamoto, U. Staub, K. Kindo, M. Hagiwara, Y. Tanaka, A. Kikkawa, H. Toyokawa, T. Fukui, R. Kanmuri, T. Ishikawa, and H. Kitamura, Phys. Rev. B **74**, 180404(R) (2006).

[8] A. I. Smirnov, H. Yashiro, S. Kimura, M. Hagiwara, Y. Narumi, K. Kindo, A. Kikkawa, K. Katsumata, A. Ya. Shapiro, and L. N. Demianets, Phys. Rev. B **75**, 134412 (2007).

[9] T. Inami, Y. Ajiro, and T. Goto, J. Phys. Soc. Jpn. **65**, 2374 (1996).

[10] Y. Shirata, H. Tanaka, A. Matsuo, and K. Kindo, Phys. Rev. Lett. **108**, 057205 (2012); T. Susuki, N. Kurita, T. Tanaka, H. Nojiri, A. Matsuo, K. Kindo, and H. Tanaka, *ibid.* **110**, 267201 (2013).

[11] A. N. Vasiliev, O. S. Volkova, E. A. Zvereva, E. A. Ovchenkov, I. Munaò, L. Clark, P. Lightfoot, E. L. Vavilova, S. Kamusella, H.-H. Klauss, J. Werner, C. Koo, R. Klingeler, and A. A. Tsirlin, Phys. Rev. B **93**, 134401 (2016).

[12] Y. Okamoto, D. Nakamura, A. Miyake, S. Takeyama, M. Tokunaga, A. Matsuo, K. Kindo, and Z. Hiroi, Phys. Rev. B **95**, 134438 (2017).

[13] S. Kimura, Y. Sawada, Y. Narumi, K. Watanabe, M. Hagiwara, K. Kindo, and H. Ueda, Phys. Rev. B **92**, 144410 (2015).

[14] K. Y. Choi, S. Do, P. Lemmens, J. van Tol, J. Shin, G. S. Jeon, Y. Skourski, J. S. Rhyee, and H. Berger, Phys. Rev. B **90**, 184402 (2014).

[15] M. Hase, M. Matsumoto, A. Matsuo, and K. Kindo, Phys. Rev. B **94**, 174421 (2016).

[16] S. Lee, W.-J. Lee, J. van Tol, P. L. Kuhns, A. P. Reyes, H. Berger, and K.-Y. Choi, Phys. Rev. B **95**, 054405 (2017).

[17] M. Hase, T. Yang, R. Cong, J. Lin, A. Matsuo, K. Kindo, K. Ozawa, and H. Kitazawa, Phys. Rev. B **80**, 054402 (2009).

[18] Z. W. Ouyang, Y. C. Sun, J. F. Wang, X. Y. Yue, R. Chen, Z. X. Wang, Z. Z. He, Z. C. Xia, Y. Liu, and G. H. Rao, Phys. Rev. B **97**, 144406 (2018).

[19] Z. He, J. I. Yamaura, Y. Ueda, and W. D. Cheng, Phys. Rev. B **79**, 092404 (2009).

[20] Y. C. Sun, Z. W. Ouyang, J. F. Wang, Z. X. Wang, Z. C. Xia, and G. H. Rao, Eur. Phys. J. Plus **131**, 343 (2016).

[21] M. Touaiher, K. Rissouli, K. Benkhouja, M. Taibi, J. Aride, A. Boukhari, and B. Heulin, Mater. Chem. Phys. **85**, 41 (2004).

[22] M. Sánchez-Andújar, S. Yáñez-Vilar, J. Mira, N. Biskup, J. Rivas, S. Castro-García, and M. A. Señarís-Rodríguez, J. Appl. Phys. **109**, 054106 (2011).

[23] J. Sannigrahi, S. Giri, and S. Majumdar, J. Phys. Chem. Solids **101**, 1 (2017).

[24] E. E. Sauerbrei, F. Faggiani, and C. Calvo, Acta Crystallogr., Sect. B: Struct. Crystallogr. Cryst. Chem. **30**, 2907 (1974).

[25] Z. He, J. I. Yamaura, Y. Ueda, and W. D. Cheng, J. Solid State Chem. **182**, 2526 (2009).

[26] R. Chen, J. F. Wang, Z. W. Ouyang, Z. Z. He, S. M. Wang, L. Lin, J. M. Liu, C. L. Lu, Y. Liu, C. Dong, C. B. Liu, Z. C. Xia, A. Matsuo, Y. Kohama, and K. Kindo, Phys. Rev. B **98**, 184404 (2018).

[27] L. B. McCusker, R. B. Von Dreele, D. E. Cox, D. Louër, and P. Scardi, J. Appl. Cryst. **32**, 36 (1999).

[28] P. Blaha, K. Schwarz, G. Madsen, D. Kvasnicka and J. Luitz, *WIEN2K* (Technische Universitat Wien, Vienna, Austria, 2001).

[29] J. P. Perdew, K. Burke, and M. Ernzerhof, Phys. Rev. Lett. **77**, 3865 (1996).

[30] U. D. Wdowik. Phys. Rev. B **84**, 064111 (2011).

[31] M. Lenertz, J. Alaria, D. Stoeffler, S. Colis, A. Dinia, O. Mentré, G. André, F. Porcher, and E. Suard, Phys. Rev. B **86**, 214428 (2012).

[32] M. E. Lines, Phys. Rev. **131**, 546 (1963).

[33] H. Shiba, Y. Ueda, K. Okunishi, S. Kimura, and K. Kindo, J. Phys. Soc. Jpn. **72**, 2326 (2003).

[34] H. Tanaka, N. Kurita, M. Okada, E. Kunihiro, Y. Shirata, K. Fujii, H. Uekusa, A. Matsuo, K. Kindo, and H. Nojiri, J. Phys. Soc. Jpn. **83**, 103701 (2014).

[35] L. J. de Jong and A. R. Miedema, Adv. Phys. **23**, 1 (1974).

[36] Y. Okamoto, M. Tokunaga, H. Yoshida, A. Matsuo, K. Kindo, and Z. Hiroi, Phys. Rev. B **83**, 180407(R) (2011).

[37] H. Ishikawa, M. Yoshida, K. Nawa, M. Jeong, S. Krämer, M. Horvatic, C. Berthier, M. Takigawa, M. Akaki, A. Miyake, M. Tokunaga, K. Kindo, J. Yamaura, Y. Okamoto, and Z. Hiroi, Phys. Rev. Lett. **114**, 227202 (2015).

[38] S. Y. Park, S. H. Do, K. Y. Choi, J. H. Kang, D. Jang, B. Schmidt, M. Brando, B. H. Kim, D. H. Kim, N. P. Butch, S. Lee, J. H. Park, and S. Ji, Nat. Commun. **7**, 12912 (2016).